Article:
Sundeep, S., Wang, J. and Griffo, A. (2021) Holistic modeling of high frequency behavior of inverter-fed machine winding, considering mutual couplings in time domain. IEEE Transactions on Industry Applications, 57 (6). pp. 6044-6057. ISSN: 0093-9994

https://doi.org/10.1109/TIA.2021.3105954

Holistic Modeling of High Frequency Behavior of Inverter-fed Machine Winding, Considering Mutual Couplings in Time Domain

Shubham Sundeep, *Student Member, IEEE*, Jiabin Wang, *Senior Member, IEEE*, and Antonio Griffo, *Member, IEEE*

***Abstract*—Prediction of the voltage distribution within the winding due to pulse-width modulated voltage impinging at the machine terminals is prevalent in literature. For this purpose, the state-of-art work employs a high-frequency model of the stator winding but fails to represent the mutual inductive and resistive couplings between the turns and the coil. Herein, this paper proposes a multi-conductor transmission line model for representing the high-frequency behavior of the stator winding. A distinctive feature of the proposed model is that it incorporates the mutual inductive and resistive coupling between the turns and the coils using a current-dependent voltage source with due account of frequency dependent parameters in the form of a ladder network. It enables the modeling of the mutual coupling of both single and multi-layer winding in the time domain without the explicit use of modal transformation, convolution integral or inverse Fourier transform. The close agreement between the simulation and the experimental results validates the proposed model of an automotive-grade 60 kW permanent magnet synchronous machine adapted in the Toyota Prius vehicle. In addition, a more intuitive analytical model is proposed to explain the voltage distribution and to characterize the peak voltage stress within the winding. The analytical model can be used to predict voltage stress as an alternative to the high-frequency model.**

***Index Terms*— Insulation Failure, Multi-Physics Based Model, Multi-Conductor Transmission Line Model, Skin and Proximity Effect, Wave Theory of Propagation.**

I. Introduction

THE voltage source inverter (VSI) fed electrical machines are more prominent in the applications such as industrial processes and automation, electrification of transport, renewable energy generations, and household appliances. The inverter-fed drives overcome the shortcomings of the electrical machines fed through supply lines by utilizing the indescribable gravimetric and volumetric power densities of the semiconductor devices. However, studies [1-2] show that the steep fronted voltage transients emerging from VSI result in excessive voltage at the machine terminal and non-linear voltage distribution within the winding, and consequently may lead to insulation failure. The peak voltage stress increases as the voltage slew rate increases, which further aggravates insulation deterioration.

To discern the cause of overvoltage and the non-linear voltage distribution, it is, therefore, important to predict the behavior of the stator winding under VSI excitation for an optimized solution without costly design iterations. For this purpose, a modeling approach representing the high-frequency (HF) behavior of the machine winding is prevalent in the literature [3-14].

Modeling of HF behavior of the stator winding involves accurate representation of wave propagation and reflection phenomenon within the winding. This can be realized by representing the winding conductors using a transmission line model. HF behavior of the winding can also be represented as a per-phase lumped parameter model [3-5] also called as behavior based model, wherein, the parameters of the model are derived from the terminal impedance measurement. However, in such models, voltage stress across individual turns and coils is inaccessible. Moreover, the physical measurement of the terminal impedance is required, which mandates the physical availability of the machine winding and hence excluding such analysis in design stages.

However, in the transmission line model, each turn or a coil is represented as a unit cell, thereby, the turn or the coil voltages are accessible, and the model is solved either in the time domain or in the frequency domain to predict voltage distribution within the winding. Also, the transmission line model can be used in the design stage, without the physical availability of the machine. The supremacy of frequency domain analysis [6-7] over the time domain [8-14] is that the partial differential voltage-current relationship in the latter is represented as an ordinary differential equation in the frequency domain. For computing the voltage stress, the input voltage pulse is decomposed into its spectral component, and then the voltage-current relationship is solved for each frequency. Later, the time domain solution is obtained using an inverse Fourier transform. This approach is expedient for considering the frequency-dependent parameters and the mutual coupling in the HF model. However, such an approach is inappropriate for the application of fast varying signals and for studies of system behavior, consisting of other components, such as inverter, possible filter, and cable, etc.

This work was supported by Engineering and Physical Sciences Research Council-EPSRC Grant EP/S00081X/1.

Shubham Sundeep, Jiabin Wang, and Antonio Griffo are with The Department of Electronics and Electrical Engineering, The University of Sheffield, Sheffield, S1 3JD UK (e-mail: ssundeep1@sheffield.ac.uk; j.b.wang@sheffield.ac.uk; a.griffo@sheffie-ld.ac.uk).

Besides the frequency domain approach, the parameters in a time domain transmission line model are either calculated using simplified analytical approaches [8] or more accurate finite element (FE) analysis [9-12]. Since the duration of steep fronted voltage transient is comparable to the wave propagation time within the winding, each turn acts as a separate conductor. Thereby, the winding can be modeled as a Multi-Conductor Transmission Line (MCTL) Model with each turn as a unit cell connected in cascade to form a winding.

Fundamentally, the MCTL model of the stator winding should include:

1. Capacitive coupling between turn and the core.
2. Capacitive coupling between the turns.
3. Frequency dependent turn resistance and inductance.
4. Frequency dependent mutual resistive and inductive coupling between the turns which may be in the same or different phases.
5. Overhang inductance and core loss representation.

Several works of literature [9-10] have proposed a model wherein, the first two features are incorporated while the turn resistance and inductance are represented as frequency independent parameters. However, the experimental measurement in [11] clearly illustrates that, as frequency increases the turn inductance decreases owing to induced eddy current within the conductors and core.

In the work in [12], the frequency dependent parameters are represented using Foster and Cauer network but neglected the mutual coupling. Albeit, the model described in [13] represented the frequency dependent parameters using RL ladder circuit, the current through each turn is assumed same, which allowed adding up the self and mutual inductance together. Such a model essentially neglects the currents through turn-to-ground and turn-to-turn capacitances, and hence, will lead to a large error at high frequency. On the other hand, the model in [14] represented the frequency dependence of the inductive and resistive coupling by embedding the capacitive coupling in the time-harmonic finite element (FE) simulations. Such an approach requires excessively large computation time and resources. In [8] the capacitance is calculated analytically using parallel plate approximation. Further, the capacitance along with the velocity of wave propagation is used to calculate frequency independent inductance without mutual coupling. Nevertheless, the literature [11] supports that the frequency dependent self and mutual resistive and inductive coupling are necessary to represent the HF behavior.

No work, to the best knowledge of the authors, has represented the frequency dependent mutual resistive and inductive coupling between the turns in the time domain analysis. Therefore, this work proposes an approach to represent such coupling lucidly.

Further investigations [10] presume that only the first few turns experience excessive voltage stress, thereby, only the first few turns are modeled as unit cells and the rest are lumped together as a series connected RL circuit. Howbeit, this study illustrates that for appropriate characterization of voltage distribution, whole winding must be represented as a MCTL model.

The following investigation shows excessive peak voltage may occur in the turns close to star-neutral of a 3-phase winding. Such voltage distribution within the winding is a result of voltage wave propagation, which can be expressed analytically to predict the peak voltage stress close to the neutral point. This analytical model is easy-to-use and does not require complex computational resources, thereby, can be used in lieu of the MCTL model. The proposed experimentally validated analytical model illustrates the voltage distribution due to VSI more realistically. A preliminary examination is conducted in [15], to study the mutual coupling, but without any analytical model representing the voltage distribution. The key contributions of this paper are:

- The frequency dependent mutual resistive and inductive coupling between the turns is represented lucidly in the time domain without using Fourier Transform and Modal transformation.
- An experimentally validated analytical approach has been proclaimed to characterize the voltage distribution and identify the location of peak voltage stress within the winding, which accounts for the transient elicited due to previous switching events.
- The experimental results indicate the critical operating conditions under which voltage stress within the winding is maximum.

The organization of this paper is as follows: Section I manifest the ignorance of the mutual inductive and resistive coupling in literature, whose solution is proposed in section II. In section III, a comparison of predicted and measured common-mode (CM) and differential-mode (DM) impedances of an automotive-grade machine validates the proposed model. The developed model is then used to identify the potential location of peak voltage stress over a complete PWM cycle. In section IV, an analytical model is proposed to characterize the voltage distribution. Concluding remarks are given in section V.

II. Multi-Conductor Transmission Line Model

Under PWM voltage excitation, the response of the machine differs from the line frequency excitation. This owes to the harmonic content present in the PWM voltage pulse. There is, therefore, a need for an HF model, which emulates the behavior of the machine. This can be realized by expressing the wave propagation/reflection phenomenon accurately, which involves a model with frequency-dependent distributed parameters. However, the inclusion of the frequency dependence of the distributed parameter model in the time domain is complex in implementation. Therefore, a lumped parameter transmission line model with a sufficiently large number of Γ or π cells is employed.

The high permeability of the stator core confines the HF components of the magnetic field within a single tooth-slot region. For a semi-closed slot, the leakage flux into the air gap is quite small, and induced eddy current in the rotor core or magnets acts as a flux barrier [10-13]. Hence, a single slot model is used for the development of the proposed model.

There is evidence in previous work [8], [11], and [13] illustrating that the rotor has the least effect on the surge voltage distribution within the stator winding. Due to the air gap and the high permeability of the rotor core, the HF flux linkage between the stator and the rotor is the least. Henceforth, the rotor is not considered in the following studies.

As a rule of thumb, the length of the winding representing each cell should be small enough such that, the space variation of the electromagnetic field within each cell along the direction of travel is negligible [16]. Considering the highest frequency component of the PWM voltage (f_{max}), up to which the model preserves its representation as a transmission line, to be 3 times the cut-off frequency (f_c), the smallest wavelength (λ_{min}) of the propagating wave along the transmission line can be expressed as [13],

$$f_{\max} = 3f_c = \frac{3}{\pi t_r} \tag{1}$$

$$\lambda_{\min} = \frac{v_w}{f_{\max}} \tag{2}$$

where, v_w is the speed of the propagating wave along the transmission line. Due to the dielectric properties of the insulation of the cable, the speed (v_w) is approximately half of the speed of light (c), and for the machine, it further reduces at least by half due to laminated effects of the core. For a machine fed through a SiC MOSFET based inverter with a typical rise time of 20 ns, the smallest wavelength of the propagating wave is 1.57 m. Herein, an 8-pole, 60 kW permanent magnet synchronous machine (PMSM) adapted in Toyota Prius vehicle is used whose specifications [17] are outlined in appendix. The stack length of the machine is 50.8 mm. Thus, representing each turn with an average length of ~0.1016 m as a cell (or, 1.57/0.1016 = 15 cells within one wavelength), offers a less complex model with acceptable accuracy. The calculation of the cell parameters representing the turn is discussed in the following sections.

A. Calculation of Turn-to-Core Capacitance

The turn-to-core capacitance is calculated using the electrostatic field solver of the ANSYS software package. The field solver excites the turns sequentially with 1 V and others kept at 0 V. Then, the solver computes the DC current flowing through the lossy dielectric materials. Using FEM, the solver solves (3) for scalar electric potential (φ) for a given charge distribution (ρ).

$$\nabla \cdot \left(\varepsilon_r \varepsilon_0 \nabla \varphi \right) = -\rho \tag{3}$$

where, ε_0 and ε_r are the permittivity in free space and relative permittivity of insulation materials, respectively. Using (3), the solver computes the capacitance matrix (c) that is further used to calculate the turn-to-core capacitance (C_{i0}),

$$C_{i0} = 2 \cdot \sum_{j=0}^{N_t} c_{ik} \tag{4}$$

where, c_{ik} is the partial capacitance between turns i and k, and c_{i0} is the partial capacitance between turn i and the core. An additional factor 2 is added to accounts for the capacitance between both the conductors of the turn and the core. During FEM analysis, the laminated core is assumed to be at zero scalar electric potential.

B. Calculation of Turn-to-Turn Capacitance

The turn-to-turn capacitance is derived from the capacitance matrix calculated by the field solver. The turn-to-turn capacitance (C_{ik}) is calculated here as,

$$C_{ik} = -c_{ik} \tag{5}$$

In the overhang region, due to the absence of the iron core, the turn-to-core capacitance is neglected. However, the turn-to-turn capacitance in the overhang region per side is assumed equal to the slot region based on the estimated overhang length. Thus, (5) is updated as,

$$C_{ik} = -2c_{ik} \tag{6}$$

An additional factor 2 is added further, to accounts for the turn-to-turn capacitance for both conductors of a turn.

C. Calculation of Turn Inductance and Resistance

For the calculation of turn inductance and resistance, the eddy current field solver from ANSYS software package is used. After defining the slot geometry, the solver computes the AC magnetic field induced due to current excitation in each turn. The software excites each turn successively with an AC current source and computes the current density within the conductor and the resultant magnetic field, considering skin and proximity effects. The software uses FEM to calculate vector magnetic potential (A) and electric potential (ϕ) using (7),

$$\nabla \times \frac{1}{\mu}\left(\nabla \times A\right) = \pi\left(\sigma + j\omega\varepsilon\right)\left(-j\omega A - \nabla\phi\right) \tag{7}$$

where, μ and ε are the permeability and permittivity of the materials, respectively, σ is the conductivity and ω is the frequency of excitation. To account for the eddy current effects, the resistance and the inductance of the turn are calculated over six frequencies (50, 1k, 10k, 100k, 1M, and 10M) Hz. The solver generates the impedance of the turns as six matrices for each frequency excitation, wherein, the diagonal elements represent the impedance of the turn and the off-diagonal elements represent the mutual coupling between two turns. The finite element analysis of the slot model provides the impedance of a conductor within a slot. To account for the impedance of a turn, the parameters are doubled. Due to the skin and proximity effect, the resistance and inductance are a non-linear function of frequency. To accurately reproduce the transient voltage, the frequency dependence of the parameters must readily be incorporated.

This is realized by approximating the non-linear variation of the parameters with a rational function using vector fitting [18] where the frequency response of turn impedance $Z(s)$ is approximated as;

$$Z(s) \approx \sum_{x=1}^{m} \frac{c_x}{s - a_x} + d + se \tag{8}$$

where, a_x and c_x are the poles and residues of the impedance respectively. Vector Fitting uses the least square method that iteratively relocates the initial set of poles to a better location and ensures a stable pole using pole flipping. The pole residue

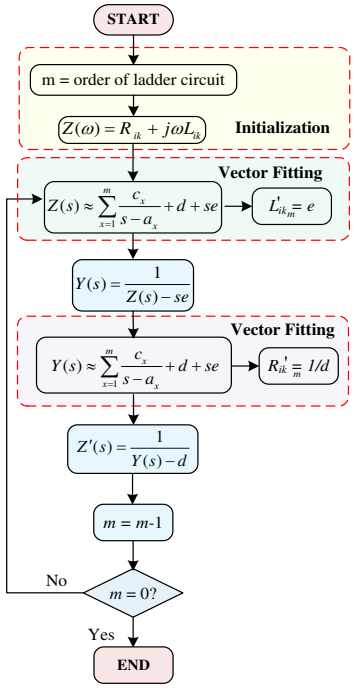

Fig. 1: Proposed procedure for the development of the ladder circuit using frequency response.

form is expressed further as a ladder circuit [16] that represents the rational function as a linear circuit. Fig. 1 proposes the procedure to calculate the parameters of the ladder circuit for self impedance (R_{ii} & L_{ii}) of turn i and, mutual coupling (R_{ik} & L_{ik}) between turns i and k. Herein, R'_{ik_n} & L'_{ik_n}, (n = 1,2, …, m) represents the parameters of the m^{th} order ladder network used to represent the frequency-dependent R_{ik} & L_{ik}. For calculating the parameters of self-impedance of turn i, $k = i$ in Fig. 1. Fig. 2 compares the frequency response of the ladder circuit used to represent the self-impedance for turn 1 and the impedance calculated using FEM. The frequency response of the ladder circuit is in close agreement with the FEM results. Hence, it can be used to represent a turn with eddy effects. The ladder circuit representing the self-inductance and resistance is illustrated in Fig. 3.

D. Representation of Mutual Inductance and Resistance between the Turns

The off-diagonal elements of the impedance matrix represent the mutual inductive and resistive coupling between two turns.

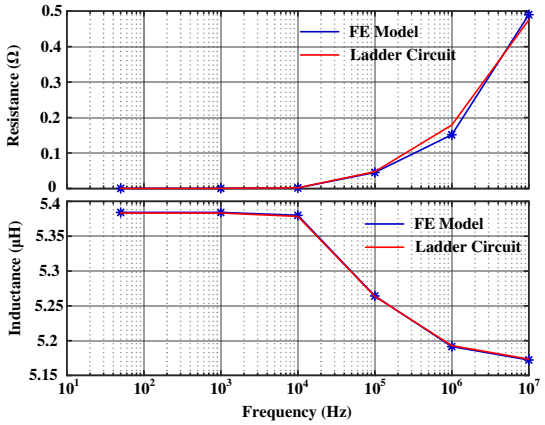

Fig. 2 Comparison of frequency-dependent resistance and inductance of a turn conductor from the FE model and frequency response of the ladder circuit.

In [13], the authors assumed that the current in each turn of the coil is the same and consequently, this allows grouping the mutual inductance and resistance of the turn in the self-impedance. However, this assumption is only valid, if the current through the capacitances is considered negligible.

To incorporate the frequency-dependent mutual inductive coupling between the turns, modal transformation [19] can be used, which diagonalizes the impedance matrix and eliminate the mutual coupling term. However, the frequency dependence of the mutual inductive coupling engenders a frequency-dependent modal transformation matrix, which increases further complexity. Instead, the mutual coupling term can be included in the model more lucidly, by using current-dependent voltage sources. Due to mutual coupling between turns i and k, the turn voltage can be mathematically expressed as;

$$V_i = \underbrace{\left(R_{ii} I_i + L_{ii} \frac{dI_i}{dt}\right)}_{V_{ii}} + \sum_{\substack{k=1 \\ i \neq k}}^{N_t} \underbrace{\left(R_{ik} I_k + L_{ik} \frac{dI_k}{dt}\right)}_{V_{ik}} \qquad (9)$$

where, V_i is the i^{th} turn voltage, I_i is the i^{th} turn current, and I_k is the k^{th} turn current. The first term (V_{ii}) in (9) represents the i^{th} turn voltage due to self-impedance. The second term (V_{ik}) in (9) represents the turn voltage due to mutual coupling between the turns and is represented as a current controlled voltage source, as can be seen in Fig. 3. The i^{th} turn voltage due to current in k^{th} turn (I_k) is calculated by injecting the current I_k through a ladder circuit representing the mutual coupling between the turn i & k. Similarly, the voltage drop due to mutual coupling with the

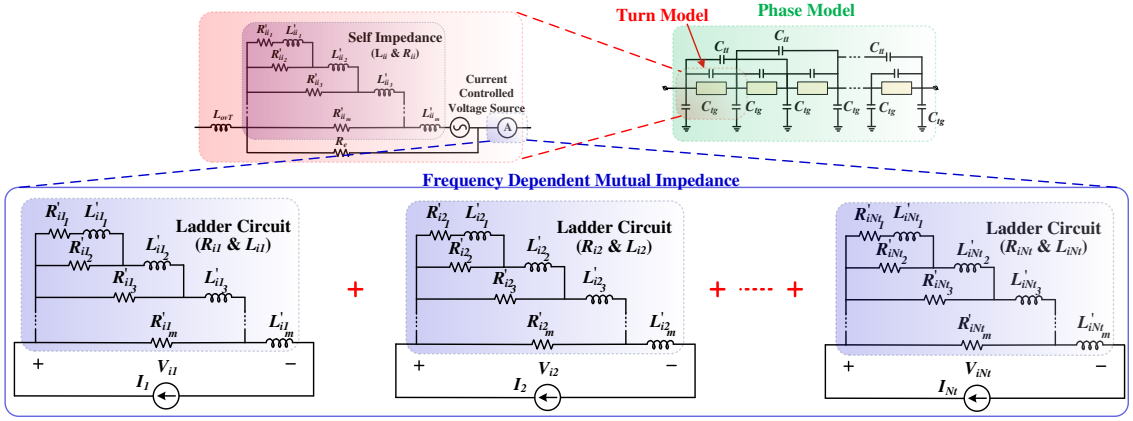

Fig. 3 MCTL model of a phase winding representing the frequency dependent self-impedance and mutual coupling between the turns.

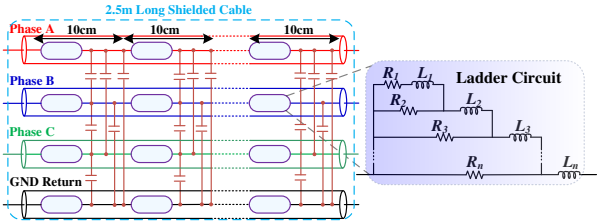

Fig. 4 HF Model of 2.5m long unshielded cable

other turns is calculated and then added together to represent the current controlled voltage source. Thus, for N_t number of turns in a coil, 1 ladder circuit is used to represent the self-impedance and N_{t-1} ladder circuits are used to represent mutual coupling for the remaining N_{t-1} turns. Herein, the stator winding has 11 turns per coil. So, for each turn model, 11 ladder circuits are used.

E. Calculation of Overhang Inductance

The winding inductance in the overhang region is assumed constant and equally distributed among the turns. This assumption is based on the experimental evidence presented in [11]. The inductance is calculated [13] from (10) as,

$$L_{ovT} \cong k_r \cdot \frac{1}{N} \cdot \left(\mu_0 N^2 \cdot \left(\frac{2}{P} \right) \cdot \lambda_b \cdot l_{ov} \right) \tag{10}$$

where, k_r accounts for the reduction in inductance due to skin effect, P is the number of pole-pairs, N is the total number of turns per phase, λ_b is geometry coefficient and l_{ov} is the length of turn in the overhang region. Herein, k_r ≈0.3, and L_{ovT} calculated from (10) is 2.8μH.

F. Calculation of Core Loss Resistance

To account for the lamination effect of the core the permeability of the stator core is assumed zero. Thereby, the losses in the core is represented as an additional resistor. An empirically defined curve [20] between the core loss resistance and the stator outer diameter is used to find the resistance. The outer diameter of the stator [17] used in this analysis is 16.19 cm. Therefore, from the curve, the core loss resistance per phase is 2 kΩ. With 11 turns per coil and 8 series coils per phase, the core loss resistance per turn is 22.73 Ω.

The stator sample [17] used in the experimental setup has 11 turns per coil and 8 series coils per phase. Therefore, 11 turn models are connected in series to build one coil model, further,

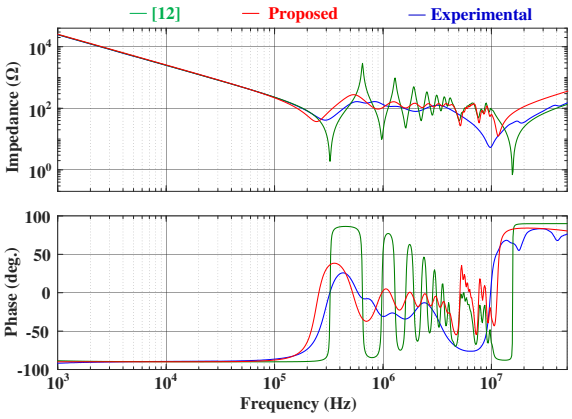

(a)

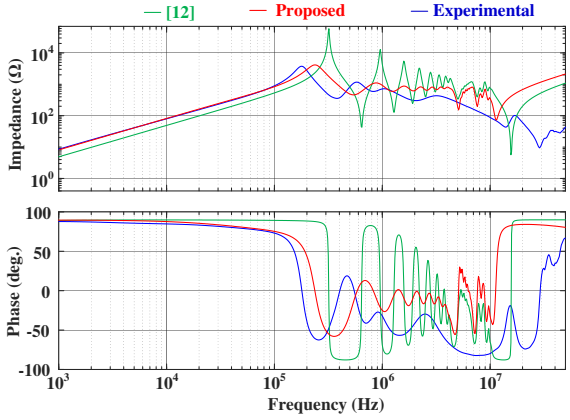

(b)

Fig. 6 Impedance comparison between actual machine (experimental) and the proposed MCTL model (simulation), (a) CM impedance, (b) DM impedance.

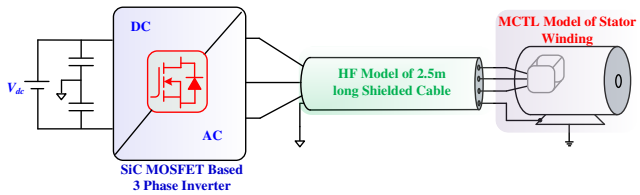

Fig. 5 Schematic representation of MCTL model of a stator winding fed by a SiC MOSFET based inverter through the HF model of cable.

8 coil models are connected in series to form a phase model.

G. Cable Model

The MCTL modeling technique and process are also applicable to cables. In this study, an HF model of a 2.5 m, 4-wire shielded cable is developed whose parameters are outlined in the appendix. The model consists of 25 cascaded Γ cells, each representing 10 cm length of the conductors. However, since there is no mutual coupling between the cascaded cells, the complexity of the circuits is greatly reduced. FEM is used to calculate the frequency-dependent impedance of the conductors and the capacitive coupling between them. Akin to the stator winding, the frequency-dependent parameters of the conductors are modeled as a ladder circuit and consequently, a ladder circuit along with the capacitance between the conductors constitutes one cell, which represents 10 cm of the cable. The HF model of the cable is shown in Fig. 4.

III. Result and Discussion

The MCTL model of the stator winding established using the technique and procedures described in section-II has been employed to predict the CM and DM impedances of the machine and the results are compared with measurements over a wide range of frequencies. To study the voltage distribution due to voltage surge impinging at the machine terminals, the combined 3-phase model, consisting of the cable and the stator winding shown in Fig. 5 is employed. The key specification of the machine is adapted from [17] and outlined in the appendix.

A. Common Mode and Differential Mode Impedance Comparison

Fig. 6 compares the measured and predicted CM and DM impedances of the stator winding. The impedances of the actual stator winding are measured using the OMICRON Lab

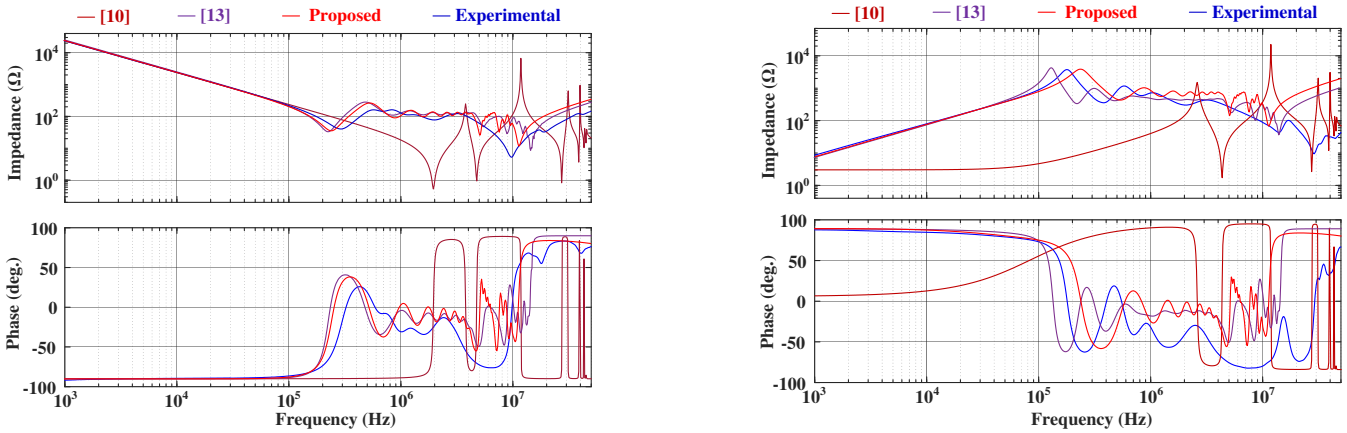

Fig. 7 Impedance comparison between actual machine (experimental) , the proposed MCTL model (simulation), and the models available in the literature [10, 13], (a) CM impedance, (b) DM impedance.

manufactured BODE 100 impedance analyzer over the frequency range of 1 kHz to 50 MHz, while the predicted impedances are obtained using the frequency analysis tool in the MATLAB/Simulink environment. To demonstrate the potency of the mutual coupling considered in the proposed MCTL model, the CM and DM impedance of a MCTL model ignoring the mutual coupling is compared. Predictably, the model [12] that ignored the mutual coupling, has low DM impedance at low frequency. Also, the model exhibits multiple resonance and anti-resonance which is not present in the experimental measurement.

In [10], only the first five turns are represented as a transmission line cell and the rest are modeled as lumped parameters. The first anti-resonance frequency in CM impedance (see Fig. 7-a) and first resonance frequency in DM impedance (see Fig. 7-b) are predominantly influenced by the turn self-inductance and the turn-to-core capacitance. As only the capacitance of the first five turns is considered, the capacitive effect of the winding is not fully represented, and consequently, it shifts towards a higher frequency. Also, the turn self-inductance and the resistance are independent of frequency and the parameters are calculated at 5 MHz frequency. However, due to skin and proximity effects, these parameters are a function of frequency. Therefore, the DM impedance in Fig. 7-b of the model is very low as compared to the experimentally measure impedance until 2 MHz.

In [13], the frequency dependent parameters of the turn are represented as ladder circuits. However, the method assumes that the current through each turn of a coil is the same, which allows to include the mutual-impedance of the turn into the self-impedance. Hence, the CM impedance in Fig. 7-a, and DM impedance in 7-b is close representative of the experimentally measured impedance. However, this approach cannot be used to model the multi-layer winding.

As is evident, the impedance of the model with mutual coupling is in close agreement with the experimental measurement. This confirms that the proposed model is a close representation of the actual stator winding. The low frequency impedance of the proposed model best fits the experimentally measured impedance. However, the drawback of the proposed model lies in its large computational time and resources.

Small differences, however, exist due to a number of uncertainties in the modeling process. First, in a random wound machine, the exact locations of conductors are unknown and the assumption has to be made for the conductor layout in the FE computations. This would inevitably affect the capacitive and magnetic couplings, as they are position dependent. The effects of core loss and the end winding are estimated and they may also introduce a small discrepancy. In addition, the material properties, such as permittivity and permeability, used in the FE analysis may also differ slightly from those in the machine.

B. Voltage Stress in Simulation Environment

In the previous section, the proposed model is validated in the frequency domain. Further, the model is used to predict the voltage distribution under single voltage pulse excitation. It is well documented in the literature [7-14] that when a single voltage pulse impinges the machine terminal, the voltage distributes non-linearly, with peak voltage stress across the first few turns of the winding. In the same vein, the proposed model is excited with a voltage pulse at phase A terminal through the cable model with respect to the other two phases, wherein, the coil-to-core voltage is shown in Fig. 8. As shown, the voltage distributes non-linearly with peak voltage stress at the first coil. The voltage soar to 974 V, which is 73.93% higher than the DC link voltage (560 V). As compared to HF oscillation in the first coil, other coils oscillate at low frequency with minimum voltage stress across the last coil close to the neutral point. However, this occurs when only one phase is switched. During normal operation, the PWM voltage pulse impinges at all three phase terminals. The switching transients emerging from voltage pulse at different phases overlap each other, thereby,

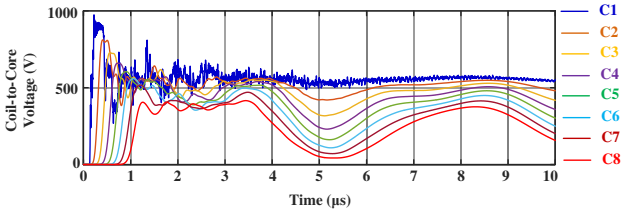

Fig. 8 Coil to core voltage under single voltage pulse excitation at phase A terminal.

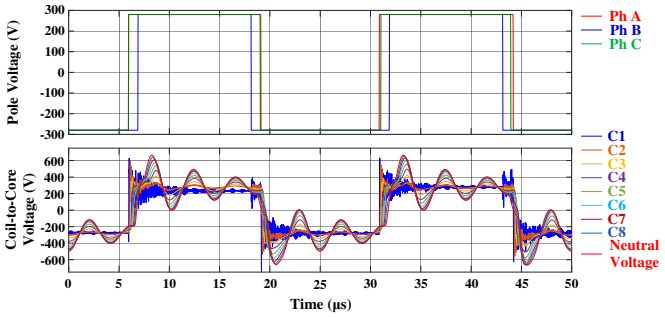

Fig. 9 Simulation result of coil-to-core voltage under PWM voltage excitation.

the voltage stress redistributes. As is illustrated, Fig. 9 shows the coil-to-core voltage under inverter operation at 0.1 modulation index and 40 kHz switching frequency. Except for the first coil, the remaining coil-to-core voltages oscillate at 227 kHz, which is the first anti-resonance frequency of the stator winding in the CM impedance. Further, in contrast to the literature [7-14], the peak voltage stress occurs across the coil close to the neutral point. Therefore, special attention is required while designing the insulation of the coil close to the neutral point.

C. *Experimental Validation of Voltage Stress*

To study the voltage distribution within the stator winding due to high slew rate voltage pulses, a SiC MOSFET based three-phase inverter is used. The SiC MOSFET is a CREE manufactured C2M0040120 with 1200V rated voltage and 60A rated drain current. To keep the studies more representative of the infield scenarios, the stator winding under investigation is an 8 pole, 560V (DC link voltage), 60 kW interior permanent magnet synchronous machine employed in the Toyota Prius vehicle. The stator winding is fed through a 4 wire cable connected between the inverter and the stator winding. The detailed specification of the stator winding and the cable is outlined in the appendix The experimental rig used in this study is illustrated in Fig. 10

At the inverter end, the potential earth wire is connected to the midpoint of the DC link and the other end is connected to the core of the machine. To illustrate the wave propagation and voltage distribution within the winding, the voltage at the neutral point, and the phase A terminal is measured with respect to the core of the machine and is compared with the voltage at the phase A terminal of the inverter output with respect to the mid-point of the DC link. These voltage waveforms are

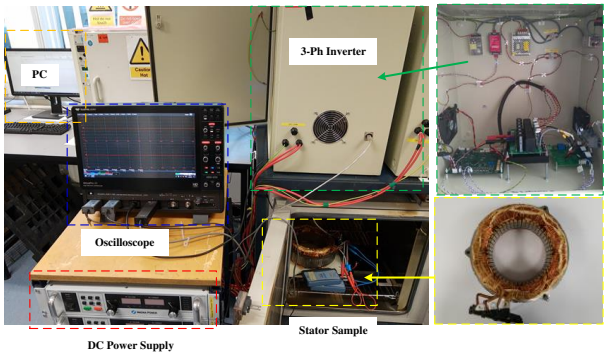

Fig. 10 Experimental rig illustrating Toyota manufactured stator sample fed by 3-phase MOSFET based inverter through 2.5 m shielded cable

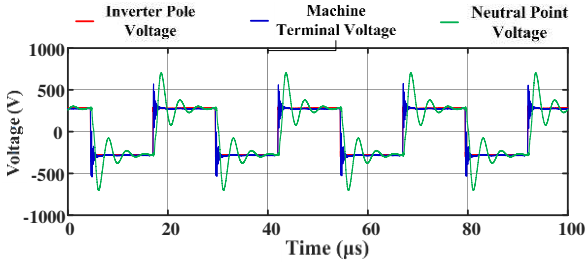

Fig. 11 Experimentally measured coil-to-core voltage under PWM voltage excitation.

acquired by Teledyne Lecroy manufactured 100 MHz bandwidth, 1400V, ADP305 high voltage active differential probes. Similar voltage oscillations can also be seen in the experimental results illustrated in Fig. 11. During the experiment, the DC link voltage is maintained at 550V. Akin to the simulation result, the coil-to-core voltage, except the line end coil, oscillates at the anti-resonance frequency of the stator winding. The voltage across the line end coil and the core oscillates at a comparable high frequency. Also, the peak voltage stress occurs at the last coil of the winding, instead of the line end coil. The reason for the damped voltage oscillation at anti-resonance frequency is explored in detail in section IV.

D. *Voltage Distribution under Different Turn Location*

The relative position of turns within the winding is also a prominent factor in determining the voltage stress across the turn insulation. In random wound winding, the first turn of a coil may be in proximity with the last turn. If this occurs, then full coil voltage will appear across the turn insulation. Fig. 12 depicts two different distribution of turns of line end coil within the slot. In case I, the second turn is placed next to the first one and the third turn is placed adjacent to the second turn. In case

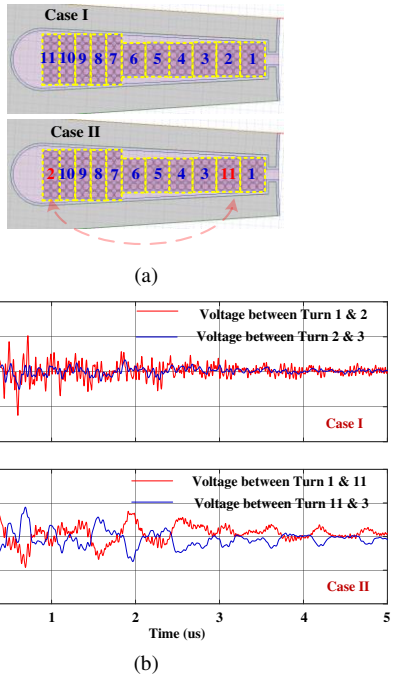

Fig. 12 Peak voltage stress across the turn insulation. (a) The second turn of the line end coil is replaced by the last turn. (b) Comparison of voltage stress across the turn insulation when the second turn of the line end coil is replaced by the last turn.

II, the second turn is replaced by the last turn of the coil (11th turn). Under the same voltage excitation at the phase A terminal, the maximum voltage stress across the turn insulation between turns 1 and 2 is 375 V, which is 67 % of the DC link voltage, which increases by two folds in case II. Also, in case I, the voltage stress across the insulation between turns 2 & 3 is 160 V, which increases by 5 times in case II. Thus, if the distribution of the turns within a slot is unconstrained, then full coil voltage may appear across the turn insulation. Therefore, the turn insulation should be designed carefully to withstand 2-3 times of DC-link voltage.

IV. Proposed Analytical Model for Voltage Distribution

Notwithstanding the fact that the first few turns are stressed, the previous section shows that it is the groundwall insulation close to the neutral point, which is most stressed. The studies in the literature [7-14] are limited to the single voltage pulse excitation at one phase with the other two connected to the ground. Therefore, it ignores the voltage distribution due to the transient overlap elicited from the previous excitation as well as excitation at the other two phase terminals. Illustratively, Fig. 8 shows the coil-to-core voltage when Phase A is switched from –ve DC link to +ve DC link with the other two phases remains connected to the –ve DC link terminal. With the absence of voltage excitation at the other two phase terminals, the first coil is most stressed, which is prevalent in literature [7-14].

A. Travelling Wave Theory and its Superposition.

The PWM voltage excitation is a spectrum of waves impinging the machine terminals. Therefore, the peak voltage stress at the neutral point can be well understood using travelling wave theory.

Consider a uniform string of length l extended in x-direction, with fixed ends between points a ($x = 0$) and b ($x = l$). Let a sinusoidal mechanical wave travels from a to b, expressed as,

$$y(x,t) = Y \sin\left(\omega t - \frac{\omega x}{\vartheta}\right) \tag{11}$$

where, Y is displacement magnitude from mean position, ω is the angular frequency, ϑ is the velocity of propagation in x-direction, and t is time. Similarly, another wave travelling in the opposite direction can be expressed as,

$$y(x,t) = Y \sin\left(\omega t - \frac{\omega(l-x)}{\vartheta}\right) \tag{12}$$

The resultant displacement of a particle of the string is the superposition of two waves and is expressed as,

$$y(x,t) = 2Y \cos\left(\frac{\omega}{\vartheta}\left(\frac{l}{2} - x\right)\right) \sin\left(\omega\left(t - \frac{l}{2\vartheta}\right)\right) \tag{13}$$

Thus, the particle displacement can be expressed as a standing wave, which is the superposition of two coherent travelling waves, travelling in the opposite direction. From (13), the particle at the mid of the string ($l/2$) displaces maximum and the fixed ends remain at the mean position. Thus, the standing waveforms nodes at the ends, and an antinode at the mid of the string, thereby, the string vibrate in a normal mode.

Nevertheless, the mechanical wave travelling along the string can be compared with the voltage waves travelling along with the coils. The PWM voltage wave impinging at machine terminals can be considered as travelling waves, which superposes to create standing waves. As illustrated in Fig. 6-a, the damping at the anti-resonance frequency is minimum. Thus, upon PWM voltage excitation, the voltage waves oscillating at anti-resonance frequency endure longer, thereby, the neutral point voltage oscillates at this frequency. Consider a voltage wave of amplitude V_m and oscillating at frequency ω impinges machine terminal at time τ_A, travelling towards neutral point. Corollary to the aforementioned discussion, the wave can be expressed mathematically as,

$$v_{A_{ac}}(x,t) = V_m e^{-\zeta(t-\tau_A)} \sin\left(\omega(t-\tau_A) - \frac{\omega x}{\vartheta}\right) \tag{14}$$

where, ϑ is velocity of propagation in x direction and ζ is the damping factor representing the damped voltage oscillations. Similarly, the voltage waves impinging phase B and C at time τ_B and τ_C are expressed as,

$$v_{B_{ac}}(x,t) = V_m e^{-\zeta(t-\tau_B)} \sin\left(\omega(t-\tau_B) - \frac{\omega(l-x)}{\vartheta}\right) \tag{15}$$

$$v_{C_{ac}}(x,t) = V_m e^{-\zeta(t-\tau_C)} \sin\left(\omega(t-\tau_C) - \frac{\omega(l-x)}{\vartheta}\right) \tag{16}$$

where, l is twice the length of phase winding. Apart from the damped sinusoidal oscillation, the coil-to-core voltage has DC component which depends on the switching states of the phases. If S_z (where, $z = A, B, C$) represents the switching states of the three phases such that, $S_z = 1$ when the upper switch of phase leg is ON and $S_z = 0$ when the lower switch of phase leg is ON, then, the DC component is represented as;

$$v_{z_{dc}}(x,t) = \begin{cases} \frac{V_{DC}}{6}; & S_z = 1 \\ -\frac{V_{DC}}{6}; & S_z = 0 \end{cases} \qquad \forall\ z = A,B,C \tag{17}$$

where, V_{DC} is the DC link voltage. Thus, the voltage at any arbitrary location in the coil with respect to the core is the superposition of the three travelling waves with a DC offset. Notably, in a space vector PWM (SVPWM) technique, τ_A-τ_B and τ_B-τ_C are the dwell time of the active space vectors, which depends on the switching frequency, modulation index, and phase angle (θ). Therefore, the voltage distribution is a function of the aforementioned factors.

Thus, using (14-17), the neutral-to-core voltage can be expressed analytically. It is noteworthy that, the analytical model does not account for the overlap of voltage transients elicited from the previous switching event with that of the present switching event. Therefore, (14-17) must be revised to account for such effects.

B. Analytical Model with Non-Zero Initial Condition

The voltage oscillations at the neutral point is a damped sinusoidal oscillation, which can be approximated as a second order system response. The time domain step response of a second order system with the non-zero initial condition is [21],

$$y(t) = Y\left(1 - \sqrt{1+\left(\frac{\zeta}{\omega}\right)^2}\, e^{-\zeta t}\cos\left(\omega t + \tan^{-1}\left(\frac{\zeta}{\omega}\right)\right)\right) - y_0\sqrt{1+\left(\frac{\zeta}{\omega}\right)^2}\, e^{-\zeta t}\cos\left(\omega t + \tan^{-1}\left(\frac{\zeta}{\omega}\right) + \phi_0\right) \quad (18)$$

where, ζ is damping factor, ω is damped frequency of oscillation, Y is the magnitude of undamped sinusoidal oscillation, y_0 and Φ_0 are initial magnitude and phase. Henceforth, (14-16) can be transformed using (18), to express the damped sinusoidal component of the neutral-to-core voltage (v_N) with the non-zero initial condition as,

$$v_{A_{ac}}(t) = v_{A_m}\sqrt{1+\left(\frac{\zeta}{\omega}\right)^2}\, e^{-\zeta(t-\tau_A)}\sin\left(\omega(t-\tau_A) + \tan^{-1}\left(\frac{\zeta}{\omega}\right) - \frac{\pi}{2}\right) + v_{A_0}\sqrt{1+\left(\frac{\zeta}{\omega}\right)^2}\, e^{-\zeta(t-\tau_A)}\sin\left(\omega(t-\tau_A) + \tan^{-1}\left(\frac{\zeta}{\omega}\right) + \phi_{A_0} - \frac{\pi}{2}\right) \quad (19)$$

$$v_{B_{ac}}(t) = v_{B_m}\sqrt{1+\left(\frac{\zeta}{\omega}\right)^2}\, e^{-\zeta(t-\tau_B)}\sin\left(\omega(t-\tau_B) + \tan^{-1}\left(\frac{\zeta}{\omega}\right) - \frac{\pi}{2}\right) + v_{B_0}\sqrt{1+\left(\frac{\zeta}{\omega}\right)^2}\, e^{-\zeta(t-\tau_B)}\sin\left(\omega(t-\tau_B) + \tan^{-1}\left(\frac{\zeta}{\omega}\right) + \phi_{B_0} - \frac{\pi}{2}\right) \quad (20)$$

$$v_{C_{ac}}(t) = v_{C_m}\sqrt{1+\left(\frac{\zeta}{\omega}\right)^2}\, e^{-\zeta(t-\tau_C)}\sin\left(\omega(t-\tau_C) + \tan^{-1}\left(\frac{\zeta}{\omega}\right) - \frac{\pi}{2}\right) + v_{C_0}\sqrt{1+\left(\frac{\zeta}{\omega}\right)^2}\, e^{-\zeta(t-\tau_C)}\sin\left(\omega(t-\tau_C) + \tan^{-1}\left(\frac{\zeta}{\omega}\right) + \phi_{C_0} - \frac{\pi}{2}\right) \quad (21)$$

$$v_{z_m}(t) = \begin{cases} \frac{V_{DC}}{3}; & S_z = 1 \\ -\frac{V_{DC}}{3}; & S_z = 0 \end{cases} \quad \forall\ z = A, B, C \quad (22)$$

$$v_N(t) = \underbrace{\left(v_{A_{ac}}(t) + v_{A_{dc}}(t)\right)}_{v_A} + \underbrace{\left(v_{B_{ac}}(t) + v_{B_{dc}}(t)\right)}_{v_B} + \underbrace{\left(v_{C_{ac}}(t) + v_{C_{dc}}(t)\right)}_{v_C} \quad (23)$$

where, v_{z0} and Φ_{z0} ($z = A, B, C$) is the initial magnitude and the phase of the damped sinusoidal oscillation. Henceforth, (19-23) can be used to represent the peak voltage stress, i.e. the neutral-to-core voltage within the winding.

C. Experimental Validation of Analytical Model

For using the proposed analytical model, experimental measurement of two parameters (ζ and ω) are required, wherein, ζ is the damping factor and ω is the damped frequency of oscillation. Given all the three phases are switched at the same instant with zero initial condition, the contribution of each phase towards the neutral-to-core voltage will be the same, which enables the measurement of ζ and ω. As an illustration, Fig. 13 shows neutral-to-core voltage along with the three phase pole voltage measured at 10 kHz switching frequency and 0.01 modulation index. ω can be measured directly from the waveform, whereas, ζ can be measured using (24) as,

$$\zeta = \frac{\left(\ln(V_1) - \ln(V_2)\right)}{(t_2 - t_1)} \quad (24)$$

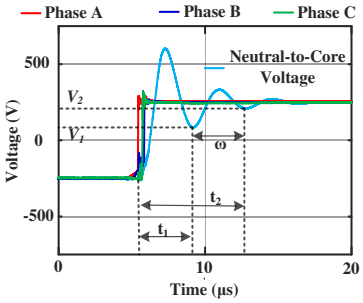

Fig. 13 Experimental measurement of damping factor (ζ) and damped frequency of oscillation (ω).

where, V_1 and V_2 are the neutral-to-core voltages measured at time t_1 and t_2 respectively. Thus, the neutral-to-core voltage can be predicted using the following measurement (Fig. 14):

1. DC link voltage (V_{DC}).
2. Pole voltage as an input for calculating instant of switching (τ_B, τ_B, and τ_C).
3. Damping factor (ζ) and damped frequency of oscillation (ω).

The efficacy of the proposed model is illustrated in Fig. 15, wherein, the measured neutral-to-core voltage is compared with the analytical model. During the experiment, the SiC based three-phase inverter with 20 ns rise time and 100V DC voltage, feeds the Toyota Prius vehicle adapted stator winding through a 2.5 m long cable. The voltage is measured at 40 kHz switching frequency with varying modulation index between 0.01 and 0.5. Only the stator winding is connected to the inverter, which limits the modulation index up to 0.5 for avoiding overcurrent. The damping factor (ζ) and the damped frequency of oscillation (ω) used during the calculation are 3.75 x 10^5 s^{-1} and 1.8347 x 10^6 $rads^{-1}$ respectively.

It is apparent from Fig. 15, the proposed analytical model can predict the neutral-to-core voltage under different modulation index with great accuracy. Following Fig. 15, below are the observations on the peak voltage stress at the neutral point:

1. The peak-to-peak voltage stress could rise up to 2.5 times DC link voltage.
2. Under a low modulation index (say 0.01), the peak-to- peak voltage stress is consistent for every switching instant.
3. The peak-to-peak voltage stress reduces with increasing modulation index.
4. Under 0.3 and 0.5 modulation index, the peak-to-peak

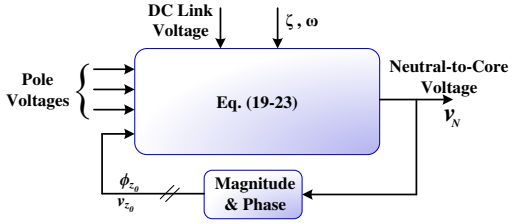

Fig. 14 Block diagram representation of the analytical model for predicting neutral-to-core voltage.

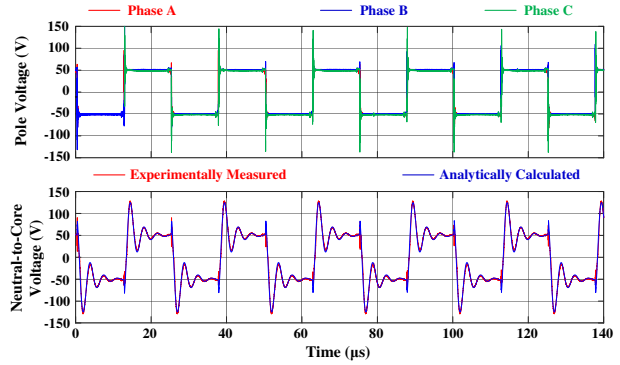

(a)

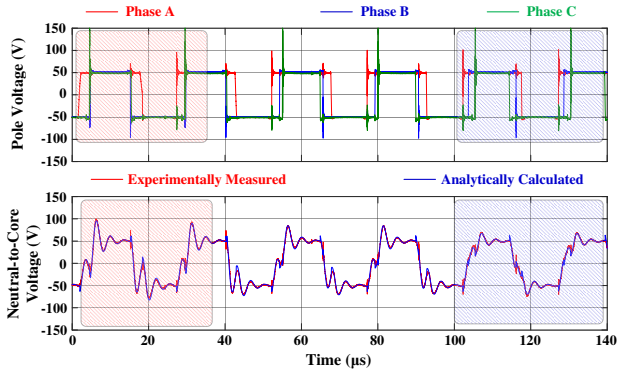

(b)

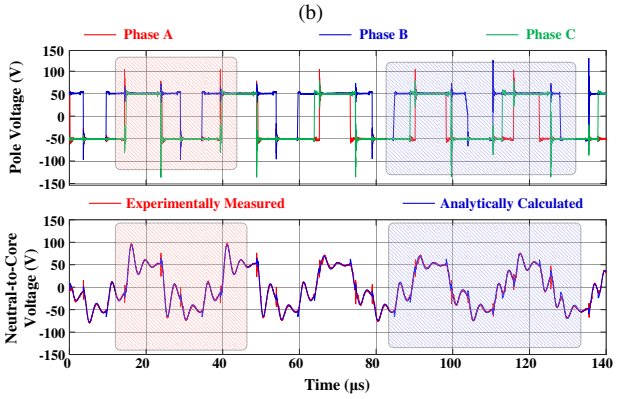

(c)

Fig. 15 Experimental validation of the proposed analytical model at 40 kHz switching frequency; (a) m = 0.01, (b) m = 0.3, (c) m = 0.5.

voltage stress varies. It is high at some switching instant and low at others.

1) Effect of Dwell Time on Neutral-to-Core Voltage

As evident, the peak of the neutral-to-core voltage largely depends on the modulation index. At a low modulation index, the switching events at all three phases occur simultaneously. Therefore, the travelling waves elicited at different phases superpose constructively and engender high voltage stress. Nevertheless, simultaneous switching also occurs at high modulation index but less likely in all 3 phases. In the regions shaded in red, two of the phases switch simultaneously, thereby, the neutral-to-core voltage rises to the DC link voltage. However, in other regions shaded in blue, the different phases switch distantly. Therefore, the neutral point voltage is less than the DC link voltage. In the SVPWM technique, the time difference between the switching of the phases (T_a and T_b) is called dwell time, which is expressed as [22],

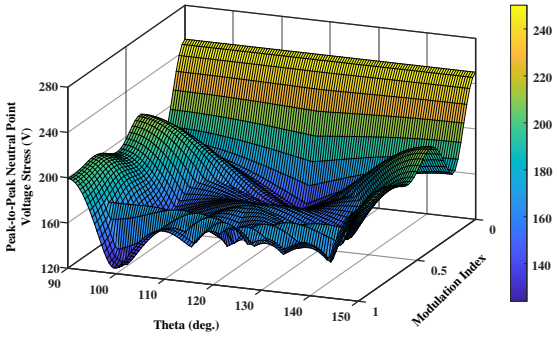

Fig. 16 Peak-to-peak neutral-to-core voltage under PWM inverter operation at 40 kHz switching frequency.

$$T_a = \frac{\sqrt{3}m}{2f_{sw}} \sin\left(\frac{\pi}{3} - \theta\right) \tag{25}$$

$$T_b = \frac{\sqrt{3}m}{2f_{sw}} \sin(\theta) \tag{26}$$

where, m is the modulation index, f_{sw} is switching frequency and θ is the angle of reference vector within a switching sector. Under a low modulation index, irrespective of θ, both T_a and T_b are small. Consequently, the switching events arrive simultaneously and the peak voltage stress is maximum at a low modulation index. Under high modulation index, T_a and T_b depend on both m and θ. Both the dwell times cannot be simultaneously short ($T_a = 0$, $T_b \neq 0$ if $\theta = \pi/3$ and $T_a \neq 0$ $T_b = 0$ if $\theta = 0$), i.e., only two phases switch simultaneously. This occurs during the change in the sector of the reference voltage vector, i.e., six times in every fundamental cycle. When this happens, as marked as the red region, the peak of the neutral-to-core voltage reaches DC link voltage. In the regions marked as blue, the dwell time is large, henceforth; the travelling waves elicited at different phases superpose destructively which restricts the neutral-to-core voltage less than the DC link voltage. Further, the experimentally validated analytical model is used to calculate the peak-to-peak voltage stress under modulation index range ($0 < m < 1$) and within one switching sector ($\pi/2 < \theta < 5\pi/6$) which is illustrated in Fig. 16. As evident, the peak-to-peak voltage stress is maximum under low modulation index as well as, when the two switching events occur simultaneously ($\theta = \pi/2$ and $\theta = 5\pi/6$).

2) Effect of Switching Frequency on Neutral-to-Core Voltage

The dwell times also depend on the switching frequency.

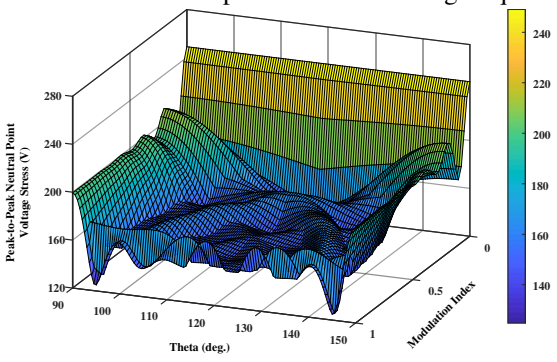

Fig. 17 Peak-to-peak neutral-to-core voltage under PWM inverter operation at 20 kHz switching frequency.

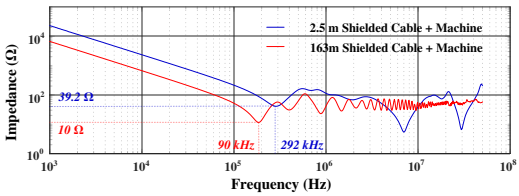

Fig. 18 Comparison between the CM impedance of the combined start winding and the cable of length 2.5m and 163m.

With inverse relation (25-26), under low switching frequency, for a given modulation index (m), the dwell times are large. Thereby, with decreased switching frequency (say 20 kHz), the peak-to-peak voltage stress decreases. Fig. 17 shows the peak-to-peak voltage stress at 20 kHz switching frequency, with varying m and phase angle (θ), wherein, except for the low m and simultaneous phase switching instant ($\theta = \pi/2$ and $\theta = 5\pi/6$), the voltage stress is less as compared to the voltage stress with 40 kHz switching frequency.

3) Effect of Cable Length on Neutral-to-Core Voltage.

The damped voltage oscillations are the key characteristics of the anti-resonance frequency. With a very long cable length, the combined anti-resonance frequency of the cable and the stator winding shift to a lower frequency range with decreased impedance. From Fig. 18, with 2.5m long cable, the anti-resonance frequency of the CM impedance of combined cable and stator winding is 292 kHz, and the impedance is 39.2 Ω, whereas, with 163m long cable, the anti-resonance frequency decreases to 90 kHz and the impedance reduces to 10 Ω. Due to reduced impedance, the damping factor of the damped voltage oscillations reduces, resulting in an increase in the peak of damped voltage oscillation. Using the proposed analytical model, with 163m long cable, the damping factor (ζ) and the damped frequency of oscillation (ω) are 1.6 x 10^5 s^{-1} and 1.1435 x 10^6 $rads^{-1}$ respectively. Fig. 19 shows the comparison of neutral-to-core voltage between experiment and the analytical model measured at 40 kHz switching frequency and 0.1 modulation index. The peak-to-peak voltage stress soar to 3.9 times the DC link voltage, which is 1.56 times higher than the voltage stress with 2.5m long cable. The peak-to-peak voltage stress at the neutral point under different modulation indexes and over one switching sector ($\pi/2 < \theta < 5\pi/6$) is shown in Fig. 20. Apparently, the voltage stress is high at the entire operating region as compared with 2.5 long cable, which owes to low ζ.

V. Conclusion

The paper has proposed an MCTL model for studying the high frequency behavior of machine windings under PWM excitation. The proposed model includes the mutual coupling between the turns within the slot using a current-controlled voltage source in the time domain. In the example considered, mutual coupling exists in the conductors of the same phase. However, the concept can also be extended to account for the mutual coupling of a double layer winding where the conductors in a slot carry currents in two different phases.

The proposed model is validated by comparing the measured and predicted CM and DM impedances. The results show in the machine under study that, during normal inverter operation,

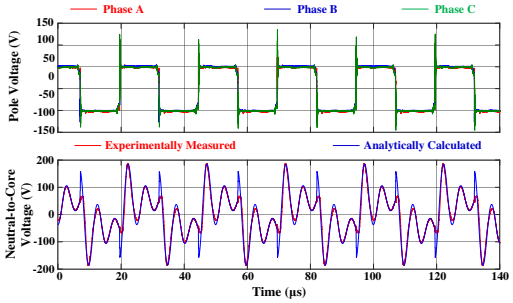

Fig. 19 Experimental validation of the proposed analytical model at 40 kHz switching frequency with 163m long cable.

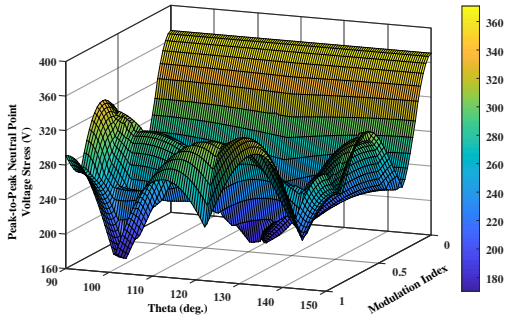

Fig. 20 Peak-to-peak neutral-to-core voltage under PWM inverter operation at 40 kHz switching frequency and 163m long cable.

the peak voltage stress occurs across the coils close to the neutral point rather than the line end coil. The physical cause and implication of the oscillation mode associated with the peak voltage have been studied comprehensively. The results show that it occurs due to the superposition of travelling voltage waves impinging at the machine terminals.

Based on the travelling wave theory, an analytical model is proposed to predict the voltage distribution within the winding under PWM inverter operation. The model accounts for the superposition of switching transients elicited due to the previous switching. In reliance on the model, the peak voltage stress occurs at the low modulation index. In addition, at high modulation index, the voltage stress is maximum at the instant of change in the switching sector, which occurs six times in a fundamental cycle. Importantly, the voltage stress increases with the switching frequency and increased cable length.

Passive filters are widely accepted in mitigating the voltage stress at the terminal ends of the machine. However, due to the difference in the location of the peak voltage stress, traditional filters cannot be used to mitigate the neutral point voltage stress. A customized passive filter based on the understanding described in this paper is required to attenuate the voltage oscillations. The voltage stress at the neutral point can be reduced by reducing the dv/dt of the common-mode voltage. This can be achieved by using multi-level inverters, or modulation techniques that minimise the CM voltage. These solutions to the inimical effect of the voltage stress will be discussed comprehensively in future work.

Appendix

The schematic diagram of the cross-section of the cable and the slot geometry of the stator core is shown in Fig. 21 and 22 respectively with the specifications mentioned in Table I and II.

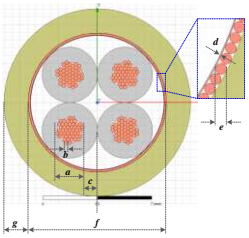

Fig. 21. Schematic diagram of the cross-section of 4-wire shielded cable.

TABLE I
PARAMETERS OF SHIELDED CABLE

Parameter	Value
Conductors	4
Conductor Diameter (*a*)	1.784 mm
No. of Strands/Conductor	40
Strand Size (*b*)	30 AWG
Thickness of core insulation (*c*)	0.9 mm
Permittivity of core insulation	2.8 F/m
Thickness of aluminium sheath (*d*)	0.02 mm
Diameter of braid strand (*e*)	0.14 mm
Inner diameter of jacket insulation (*f*)	9 mm
Thickness of jacket insulation (*g*)	1.5 mm
Permittivity of jacket insulation	4 F/m

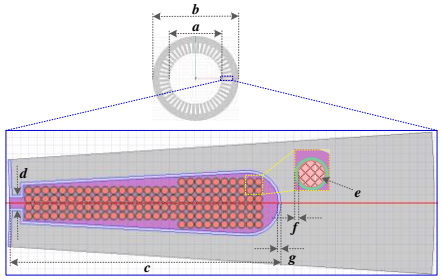

Fig. 22. Schematic diagram of the stator slots of the machine.

TABLE II
STATOR DIMENSIONS [17] AND PROPERTIES OF INSULATION

Parameter	Value
Dimension of the Stator Slots	
Inner stator diameter (*a*)	161.9 mm
Outer stator diameter (*b*)	264 mm
Stack length	50.8 mm
Depth (*c*)	30.9 mm
Slot opening (*d*)	1.88 mm
Parameters of the Stator Winding	
Number of slots	48
Series coils/Phase	8
Parallel circuits/Phase	0
Turns/Coil	11
Parallel Strands per turn	12
Cross-section area of wire (*e*)	0.52 mm^2
Resistance/Phase	0.77 Ω
Insulation Parameter of the Stator Winding	
Thickness of turn insulation (*f*)	0.025 mm
Permittivity of turn insulation	3.5 F/m
Permittivity of main-wall insulation	3.5 F/m
Thickness of ground-wall insulation (*g*)	0.35 mm
Permittivity of ground-wall insulation	3.5 F/m

ACKNOWLEDGEMENT

The authors would like to acknowledge the support from the project partner, Dr Mohamed Diab, Dr. Ian Laird and Prof. Xibo Yuan from The University of Bristol for the provision of the SiC inverter used in the experiments.

REFERENCES

[1] Yifan Tang, "Analysis of steep-fronted voltage distribution and turn insulation failure in inverter-fed form-wound AC motor," *IEEE Trans. Ind. Appl.*, vol. 34, no. 5, pp. 1088-1096, Sept.-Oct. 1998.

[2] A. H. Bonnett, "Analysis of the impact of pulse-width modulated inverter voltage waveforms on AC induction motors," *IEEE Trans. Ind. Appl.*, vol. 32, no. 2, pp. 386-392, March-April 1996.

[3] B. Mirafzal, G. Skibinski, R. Tallam, D. Schlegel, and R. Lukaszewski, "Universal induction motor model with low-to-high frequency-response characteristics," *IEEE Trans. Industry Appl.*, vol. 43, no. 5, pp. 1233 1246, Sep./Oct. 2007

[4] O. Magdun and A. Binder, "High-frequency induction machine modeling for common mode current and bearing voltage calculation," *IEEE Trans. Ind. Appl.*, vol. 50, no. 3, pp. 1780–1790, May/Jun. 2014.

[5] J. Sun and L. Xing, "Parameterization of three-phase electric machine models for EMI simulation," *IEEE Trans. Power Electron.*, vol. 29, no. 1, pp. 36-41, Jan. 2014.

[6] P.G. McLaren and H. Oraee, "Multiconductor transmission-line model for the line-end coil of large AC machines," *IEEE Proc. Part B*, pp. 149-156, May 1985.

[7] J. L. Guardado and K. J. Cornick, "A computer model for calculating steep-fronted surge distribution in machine windings," *IEEE Trans. Energy Convers.*, vol. 4, no. 1, pp. 95-101, March 1989.

[8] M. T. Wright, S. J. Yang, and K. McLeay, "General theory of fast-fronted interturn voltage distribution in electrical machine windings," in *Proc. Inst. Elect. Eng.*, pt. B, vol. 130, no. 4, pp. 245–256, July 1983.

[9] M. Pastura *et al.*, "Partial discharges in electrical machines for the more electric aircraft—Part I: A comprehensive modeling tool for the characterization of electric drives based on fast switching semiconductors," *IEEE Access*, vol. 9, pp. 27109-27121, 2021.

[10] G. Suresh, A. Toliyat, A. Rendusara, and N. Enjeti, "Predicting the transient effects of PWM voltage waveform on the stator windings of random wound induction motors," *IEEE Trans. Power Electron.*, vol. 14, no. 1, pp. 23–30, Jan. 1999.

[11] T. Humiston and P. Pillay, "Parameter measurements to study surge propagation in induction machines," *IEEE Trans. Ind. Appl.*, vol. 40, no. 5, pp. 1341-1348, Sept.-Oct. 2004.

[12] J. L. Guardado, J. A. Flores, V. Venegas, *et al.*, "A machine winding model for switching transient studies using network synthesis," *IEEE Trans. Energy Convers.*, vol. 20, no. 2, pp. 322-328, June 2005.

[13] O. Magdun, S. Blatt and A. Binder, "Calculation of stator winding parameters to predict the voltage distributions in inverter fed AC machines," in *Proc. IEEE International Symposium on Diagnostics for Electric Machines, Power Electronics and Drives (SDEMPED),* Valencia, Spain, pp. 447-453, 2013.

[14] Y. Xie, J. Zhang, F. Leonardi, A. R. Munoz, M. W. Degner and F. Liang, "Modeling and verification of electrical stress in inverter-driven electric machine windings," *IEEE Trans. Ind. Appl.*, vol. 55, no. 6, pp. 5818-5829, Nov.-Dec. 2019,

[15] S. Sundeep, J. Wang and A. Griffo, "Prediction of transient voltage distribution in inverter-fed stator winding, considering mutual couplings in time domain," in *Proc. IEEE Energy Conversion Congress and Exposition (ECCE)*, pp. 517-524, Detroit, MI, USA, 2020.

[16] H. De Paula, D. A. d. Andrade, M. L. R. Chaves, J. L. Domingos and M. A. A. de Freitas, "Methodology for cable modeling and simulation for high-frequency phenomena studies in PWM motor drives," *IEEE Trans. Power Electron.*, vol. 23, pp. 744-752, Mar. 2008.

[17] M. Olszewski (2011 Mar.). Evaluation of the 2010 Toyota Prius hybrid synergy drive system. Oak Ridge National Laboratory, USA. [Online] Available:https://info.ornl.gov/sites/publications/files/Pub26762.pdf.

[18] B. Gustavsen and A. Semlyen, "Rational approximation of frequency domain responses by Vector Fitting," *IEEE Trans. Power Del.,* vol. 14, no. 3, pp. 1052-1061, July 1999.

[19] L. M. Wedepohl, H. V. Nguyen and G. D. Irwin, "Frequency-dependent transformation matrices for untransposed transmission lines using Newton-Raphson method," *IEEE Trans. Power Syst.,* vol. 11, no. 3, pp. 1538-1546, Aug. 1996.

[20] A. Boglietti, A. Cavagnino, M. Lazari, "Experimental High-Frequency Parameter Identification of AC Electrical Motors," *IEEE Trans. Ind. Appl.*, vol. 43, no. 1, pp. 23-29, January/February 2007

[21] N. S. Nise, *Control System Engineering*, 7th ed. Hoboken, New Jersey, John Wiley & Sons, Inc., 2015.

[22] B. Wu, M. Narimani, *High-Power Converters and AC Drives*, 2nd ed., Hoboken, New Jersey, John Wiley & Sons, Inc., 2017.